Removing methylene blue from water: a study of sorption effectiveness onto nanoparticles-doped activated carbon

Removing methylene blue from water: a study of sorption effectiveness onto nanoparticles-doped activated carbon

Kehinde Shola Obayomi [a,], Sie Yon Lau [a], Abdul Zahir [b], Louise Meunier [c], Zhang Jianhua [d], Adewunmi Oluwasogo Dada [e], Mohammad Mahmudur Rahman [f, g]

[a] Department of Chemical Engineering, Curtin University, CDT 250, 98009 Miri, Sarawak, Malaysia

[b] National Textile Research Centre, National Textile University, Faisalabad, 37610, Pakistan

[c] Department of Chemical Engineering, Queen's University, Kingston, K7L 3N6, Canada

[d] Institute for Sustainable Industries and Liveable Cities, Victoria University, PO Box 14428, Melbourne, 8001, Vic., Australia

[e] Industrial Chemistry Programme, Nanotechnology Laboratory, Department of Physical Sciences, Landmark University, P.M.B.1001, Omu-Aran, Kwara, Nigeria

[f] Global Centre for Environmental Remediation (GCER), College of Engineering, Science and Environment, The University of Newcastle, Callaghan, NSW 2308, Australia

[h] Department of General Educational Development, Faculty of Science and Information Technology, Daffodil International University, Ashulia, Savar, Dhaka - 1207, Bangladesh

*Corresponding Authors

Tel.: +60168854250; +2348066967564

E-mail: obayomikehindeshola@gmail.com

Full postal address: Department of Chemical Engineering, Curtin University Malaysia, CDT 250, 98009 Miri, Sarawak.

Abstract

In this present study, silver (Ag) and titanium dioxide (TiO_2) nanoparticles were successfully deposited on coconut shell-derived activated carbon (CSAC), to synthesize a novel nanocomposite (CSAC@AgNPs@TiO_2NPs) for the adsorption of Methylene Blue (MB) dye from aqueous solution. The fabricated CSAC@AgNPs@TiO_2NPs nanocomposite was analyzed by Scanning Electron Microscope (SEM**),** X-ray Diffraction (XRD), Fourier-Transform Infrared Spectroscopy (FTIR), Transmission Electron Microscope (TEM) equipped with Energy Dispersive X-ray spectroscopy (EDS) detector, X-ray Photoelectron Spectroscope (XPS), and Brunauer–Emmett–Teller (BET). The successful deposition of AgNPs and TiO_2NPs on CSAC surface was revealed by the TEM/EDX, SEM, and XPS analysis. The mesopore structure of CSAC@AgNPs@TiO_2NPs has a BET surface area of 301 m^2/g. The batch adsorption studies were conducted and the influence of different parameters, i.e., adsorbent dose, adsorption time, initial dye concentration, pH and temperature were investigated. The nonlinear isotherm and kinetic modelling demonstrated that adsorption data were best fitted by Sips isotherm and pseudo-second-order models, respectively. The maximum adsorption capacity of MB onto CSAC@AgNPs@TiO_2NPs by the Sips model was 184 mg/g. Thermodynamic results revealed that the adsorption was endothermic, spontaneous and physical in nature. CSAC@AgNPs@TiO_2NPs revealed that MB absorption by CSAC@AgNPs@TiO_2NPs was spontaneous and endothermic. The uptake capacity of MB was influenced significantly by the presence of competing ions including, NO_3^-, HCO_3, Ca^{2+}, and Na^+. Repeated tests indicated that the CSAC@AgNPs@TiO_2NPs can be regenerated and reused six times before being discarded. The primary separation mechanism between MB dye and CSAC@AgNPs@TiO_2NPs was the electrostatic interaction. Thus, CSAC@AgNPs@TiO_2NPs was an outstanding material, which displayed good applicability in real water with ≥ 97 % removal of MB dye.

Keywords: CSAC@AgNPs@TiO_2NPs; Methylene blue; Adsorption; Surface modification; Mechanism; Comparative study

1. Introduction

Synthetic dye contamination of aqueous environments is a severe environmental concern due to their hazardous nature and removal efficiency by generally accessible treatment techniques (Priyan et al, 2022). Dyes are derivatives of aromatic hydrocarbons such as benzene, anthracene, toluene, naphthalene, xylene, and other hydrocarbons, which are highly toxic to humans and marine environments (Ifguis et al., 2022; Obayomi et al., 2021). About 7×10^5 tonnes of dyes are being produced worldwide annually, and 10 to 15% of these dyes are discharged into waste effluent during the synthesis and various industrial processes without treatment (Ivanets et al., 2022). Azo compounds contributed 65-70 % of the volume of all dye production (Rahmayanti et al., 2022; Gong et al., 2021). Due to its notable toxicity and high solubility in water, methylene blue (MB), a cationic dye majorly used in the various process industries such as textile, paper and leather, is regarded as one of the most harmful pollutants (Boughrara et al., 2022; Xue et al., 2022). Thus, wastewater treatment research is necessary to identify novel approaches and methods to decontaminate these pollutants from the aqueous environments (Jayawardena et al., 2022).

Several conventional treatment techniques, including chemical (electrochemical coagulation, photoelectric catalysis, electrochemical destruction, Fenton reactions, ozonation, advanced oxidation process, and ultraviolent radiation), biological (use of micro-organisms such as fungi, bacteria, and algae), and physical (adsorption, coagulation and flocculation, reverse osmosis, membrane separation, and ion-exchange) have been employed as a remedial action for the elimination of dyes from the wastewater effluent (Li et al., 2022; Manohara et al., 2021). The biological techniques are more cost-effective, and non-toxic, but time-consuming than the

chemical techniques, which are more effective but expensive and generate toxic secondary pollutants. (Saravanan et al., 2021; Singh et al., 2022).). Hence, physical methods are effective and economical due to their simplicity, reduced use of chemicals, easy regeneration, and great removal efficiency (Ahmed et al., 2021). Among other physical methods, adsorption has been considered the effective remediation of dyes from waste-effluent due to its operational flexibility, simplicity, cost-effectiveness, environmental friendliness, excellent adsorptive performance, ease of regeneration, and reusability (Mu et al., 2022; Obayomi et al., 2022)

Activated carbons (ACs) are mainly comprised of carbonaceous enriched materials that have the high surface area and porous structure with numerous chemical groups such as lactone, quinone, carbonyl, and phenol which make it well-known adsorbent (Jawad et al., 2022; Gul et al., 2022; Husien et al., 2022). The development of commercial AC using coal as the starting material has been widely studied, but it is limited by the non-renewable nature of coal and the cost involved (Zhu et al., 2021). However, the preparation of AC from biomass materials such as agricultural and forestry wastes, crustacean shells, wood, and many more has attracted considerable attention due to their abundance in nature, renewability, recyclability, eco-friendliness, and cost-effectiveness (Kamaraj et al., 2022; Reçber et al., 2022). Biomass-based adsorbents can be synthesized by various techniques. Biomass-based adsorbents have gained a lot of attention in recent years because of their porous structure and large surface area with numerous surface functional groups (Koyuncu, et al., 2020). Therefore, biomass-based AC is a promising adsorbent in terms of dye removal. The use of coconut shells as the starting material for AC preparation, among other biomass materials, has been considered suitable due to its low ash and high carbon content (Widiyastuti et al., 2020). However, the low selectivity of AC has limited its widespread use in the dye treatment process. Thus, additional surface modifications are necessary to improve

the adsorption capacity, by tailoring the crucial the physico-chemical properties. (Bethula et al., 2021).

Nanoparticles (NPs) have drawn a lot of attention to the scientific community due to their distinctive physiochemical characteristics, i.e., surface area to weight ratio, which results in increased kinetic and adsorption capacity (Masoudian et al., 2019). A big drawback of using NPs in wastewater treatment is the difficulty of separating and isolating dispersed NPs. It is necessary to support highly dispersed NPs on other materials such as AC, charcoal, polymers, fibres, oxides, and many others to overcome these difficulties and speed up their separation and isolation from aquatic environments (Rheima et al., 2022). Due to their numerous distinctive qualities, such as environmental compatibility, resistive to thermo-chemical degradation, affordability, large surface area, and the ability to maintain the co-characteristics of NPs and biomass-based AC simultaneously and thus decorating NPs on the surfaces of biomass-ACs have attracted tremendous research interest (Shaikh et al., 2021). The AC-based nanocomposite is one of the most significant and effective materials employed in wastewater dye remediation in recent years (Ahmed and Ansari, 2022). They belong to a brand-new category of biodegradable bio-adsorbents with ultrafine phase dispersion and promising adsorptive performance. The decoration of NPs on conventional adsorbent materials was reported to enhance their surface area, thermal properties, and effectiveness (Sunny et al., 2022).

Several researchers developed AC-based composites and studied their adsorption behaviours with MB dye. Joshiba et al., (2022) in a recent work explored the use of activated carbon doped with iron oxid3 nanoparticles for MB removal. The authors reported that the maximum adsorption capacity of MB was 357.42 mg/g. The kinetic dat were best fits to the pseudo-second-order model. The thermodynamic parameters indicated that this adsorption process was found to be

spontaneous, and exothermic. Yadav et al., (2022) also reported the use of Carbon nanotube (CNT) incorporated eucalyptus-derived activated carbon for MB treatment. The authors reported that the maximum adsorption capacity was 49.16 mg/g and the adsorption process followed D-R model. The pseudo second-order model was reported to best define the reaction kinetics involved in the reaction. Obayomi et al., (2021) also fabricated zinc oxide nanoparticles loaded on *Delonix regia*-derived activated carbon (ZnONPs-FPAC) for MB treatment. The high BET surface area of 794.48 m^2/g and mesoporous ZnONPS-FPAC developed gave a good adsorption capacity of 186 mg/g. The authors revealed that the adsorption of MB onto ZnONPs-FPAC was best described by the Freundlich model indicating surface heterogeneity, and pseudo-second-order kinetics. However, to the best of our knowledge no researchers have reported the doping of silver (Ag) and titanium oxide (TiO_2) nanoparticles on AC- derived biomass for MB treatment.

The current study aims to fabricate a novel nanocomposite (CSAC@AgNPs@TiO_2Nps) using silver (Ag) and titanium oxide (TiO_2) nanoparticles decorated on coconut shell-derived activated carbon for the removal of MB dye from the aqueous solution. The functional groups, elemental composition, crystallinity, and morphological characteristics of the prepared nanocomposite were analysed using various advanced instrumental techniques. and XRD techniques. The effect of various adsorption parameters, kinetics, and isotherms for MB onto CSAC@AgNPs@TiO_2Nps nanocomposite was studied. Furthermore, thermodynamics parameters, regenerability and reusability, thermal stability, and adsorption mechanism were also investigated. Moreover, the adsorptive performance of the prepared adsorbent was validated using real water.

2. Experimental

2.1. Materials

Coconut shells (CS) were procured from Omu-Aran Market, Kwara State, Nigeria. Chemicals, such as hydrochloride acid (HCl), aqueous silver nitrate ($AgNO_3$), Methylene blue ($C_{16}H_{18}ClN_3S$), titanium dioxide (TiO_2), sodium hydroxide (NaOH), and sodium borohydride (NaBH4), were procured from Merck (Malaysia).

2.2. Development of coconut shell-derived activated carbon (CSAC)

The CSAC was prepared according to the method proposed by Obayomi et al., (2021) with some modifications. The collected CS were thoroughly washed, sun-dried for 48 h, and then dried in an oven at 108 ^oC for another 24 h. The dried CS was carbonized in a muffle furnace at 500 ^oC and kept for 3 h at 20 ^oC/min under the nitrogen environment at a flow rate of 25 mL/min. The synthesized char was collected and cooled at 25 ^oC. The char was later subjected to chemical treatment with KOH solution at a 2:1 (g KOH/g char) weight ratio and left overnight. Following the completion of the reaction, the mixture was rinsed with 1% HCl solution and then washed several times with deionized water until the pH became constant and lied within the range of 6.5-7.0. The sample was dried at 108 ^oC for 5 h, reduced to the particle size of 212 µm and stored in the air-tight container for further use.

2.3. Fabrication of CSAC@AgNPs@TiO_2NPs nanocomposite

Initially, 90 mL of 10 mM of $NaBH_4$ was transferred into a 250 mL beaker and placed in an ice bath for 30 min under continuous stirring. Afterwards, 10 mL of 1mM of $AgNO_3$ was added dropwise. The beaker was removed from the ice bath and 0.1 g TiO_2 was added to the solution mixture and placed on a magnetic stirrer at the reaction temperature of 70 ^oC for 30 min. Thereafter, 0.5 g of CSAC was then added and the mixture containing CSAC, AgNPs, and

169 TiO_2NPs was allowed for 1 h under continuous stirring. After the reaction was completed, the
170 mixture was decanted to remove unreacted TiO_2 during the process and then oven-dried overnight
171 at 108°C. The resultant fabricated nanocomposite was labelled CSAC@AgNPs@TiO_2.

172 2.4. CSAC@AgNPs@TiO_2NPs characterization

173 The morphological structures and elemental compositions of the fabricated material were
174 investigated using the Scanning Electron Microscope (SEM, Thermo Fisher, USA). The surface
175 functional group investigation was conducted using the Fourier Transform Infrared Spectroscopy
176 (FTIR) (Thermo Fisher Nexus 670, USA). The determination of the adsorbent's surface area,
177 average pore diameter and cumulative pore volume were carried out using the Brunauer Emmett
178 and Teller (BET, BelsorpX Mini (MicrotracBEL Co., Kyoto, Japan) at 77.36 K. The powdered X-
179 ray Diffraction (Bruker, AXS D8, MA-USA) with copper radiation (Kα = 1.541 Å) was applied to
180 determine the structural and crystallographic properties of the prepared material. The fabricated
181 material's elemental composition, chemical structure and atomic electronic state were measured
182 using X-ray Photoelectron Spectroscopy (XPS, Mg Ka (1253.6 eV), Kratos Axis Ultra DLD, UK).
183 The point of zero charge (pH_{pzc}) of CSAC@AgNPs@TiO_2NPs was conducted by measuring into
184 a set of 100 mL Erlenmeyer flasks, 50 mL of 0.1 M NaCl and 0.1 g CSAC@AgNPs@TiO_2NPs.
185 The solution of different pH (2-11) was prepared with 0.1 M NaOH or 0.1 M HCl. The samples
186 were placed on the incubator shaker for 24 hours with the speed set to 140 rpm. The final pH
187 readings were recorded when the NaCl solution and the CSAC@AgNPs@TiO_2NPs
188 nanocomposite reached equilibrium at the end of the experiment. The plot of $pHi-pH_f$ vs initial pH
189 was then plotted to determine the pH_{pzc}.

190

191

2.5. Batch equilibrium adsorption performance

Methylene blue (MB) dye molecule stock solution (1000 mg/L) was prepared by measuring 1000 mg of MB dye and dissolving it in 1000 ml of ultrapure water and stored in a dark glass bottle to prevent photodegradation. The 1000 mg/L solution was then further diluted into different initial concentrations via serial dilution techniques ranging from 10–50 mg/L. Batch equilibrium adsorption studies were conducted at temperatures of 30, 40, and 50 ^{o}C in a set of different 250 mL Erlenmeyer flasks with different MB concentrations (10–50 mg/L). CSAC@AgNPs@TiO_2Nps nanocomposite (50 mg) was measured and introduced into each flask while maintaining the pH of the MB dye solution. To achieve a perfect contact between the adsorbent and adsorbate, the flasks were swirled and afterwards placed in an incubator for 180 min with constant shaker speed of 140 rpm at a predetermined temperature. Before equilibrium was reached, MB residual concentrations were taken and measured at different intervals of time (0-180 min) using UV-VIS spectrophotometer (Shimadzu UV-1601 spectrophotometer, Japan) at an absorbance wavelength 665 nm. Thus, the percentage removal of MB ($\%MB\ removal$ at different time intervals at time (t), were evaluated by the following equations:

$$MB\ removal\ (\%) = \left(\frac{C_f - C_o}{C_o}\right) \times 100 \quad (1)$$

$$q_e = \frac{(C_0 - C_e)\,V}{w} \quad (2)$$

$$q_t = \frac{(C_0 - C_t)\,V}{w} \quad (3)$$

Where, C_o, C_f,, C_e and C_t are the initial, final and equilibrium concentration (mg/L) of MB dye concentrations at equilibrium and time (t), respectively. V is the volume of solution (L) under consideration, and w is the dry adsorbent weight (g).

3. Results and discussion

3.1 Characterization of nanocomposite

3.1.1. FTIR analysis

The FTIR spectrum of CSAC and CSAC@AgNPs@TiO_2NPs are shown in Fig 1a. The broad transmittance peak at 3443 cm^{-1} is attributed to the -OH stretching due to the absorbed moisture on the surface of the adsorbents. The characteristic peaks at 2921 and 2850 cm^{-1} correspond to the symmetric and asymmetric -CH stretching within the CSAC structure (Ali et al., 2020). The sharp transmittance band at 2361 cm^{-1} represents the vibrational stretching of C=O. The transmittance peak at 1622 cm^{-1} is associated with aromatic C=C vibrations. The appearance of a transmittance peak at wavelengths ranging from 870-502 cm^{-1} shows the aromatic -CH (Nagalakshmi et al., 2015). The FTIR spectrum of CSAC@AgNPs@TiO_2NPs exhibits some considerable changes as can be seen in Fig. 1a. The presence of a very sharp transmittance band at 502 cm^{-1} corresponds to Ti-O. It can be observed from the spectra that there is no transmittance peak for Ag nanoparticles which may be due to the smaller molecular size of Ag_2O_3 that requires more excitation energy which does not lie within the IR range of FITR analysis (León et al., 2017; Mugundan et al. 2015).

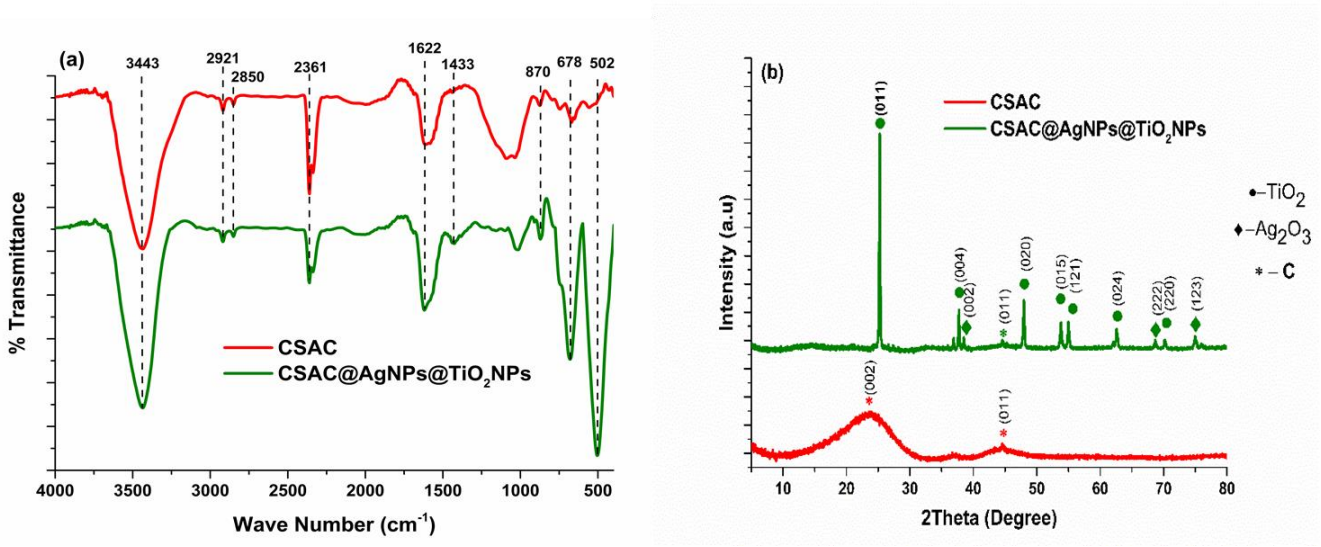

Fig. 1. (a) FTIR, (b) XRD analysis for CSAC and CSAC@AgNPs@TiO_2NPs

3.1.2. XRD analysis

The diffractograms of both CSAC and CSAC@AgNPs@TiO_2NPs are presented in Fig 1b. The broad diffraction peaks at ~23° and 44° exhibit the $Cr_{(002)}$ and $Cr_{(011)}$ of the amorphous carbon structure, respectively (Valdés-Rodríguez et al., 2022). However, no diffraction peak of $Cr_{(002)}$ at 23° can be seen in CSAC@AgNPs@TiO_2NPs, which may be due to the overlapping of the highly crystalline plane, i.e., $Cr_{(011)}$ of the TiO_2 in the CSAC@AgNPs@TiO_2NPs. The sharp diffraction peaks at 37.7, 48, 53.7, 54.8, 62.7 and 70° confirm the presence of TiO_2 in CSAC@AgNPs@TiO_2NPs. The appearance of these peaks reveals that TiO_2 is attached in the form of tetragonal-shaped Anatase (Valdés-Rodríguez et al. 2022). Likewise, the diffractogram of CSAC@AgNPs@TiO2NPs also shows the diffraction peaks at 38.4, 68.5 and 75° which are ascribed to the cubic-shaped silver (III) oxide (Ag_2O_3) (Mohammed et al., 2020). The presence of these diffraction peaks in the diffractogram of CSAC@AgNPs@TiO_2NPs confirms the successful incorporation of the Ti and Ag NPs into the AC, which is also consistent with previously reported studies (Zhang et al. 2018; Peñas-Garzón et al. 2019).

3.1.3. Morphological analysis

The SEM micrographs of CSAC showed that it has a completely disintegrated topological structure and the surface is zipped up with the ostium and heterogeneous surface cavities (Fig. S1(a-c)). However, AgNPs and TiO_2NPs (Fig. S1(d-f) exist in the form of agglomerates and are deposited non-uniformly in the porous structure of the CSAC (Fig. S1(d-f)). (Kaya, et al., 2018; Anisuzzaman et al. 2015).

3.1.4. TEM analysis

The TEM images (Fig. 2a-c) of CSAC revealed smooth surface with high graphitization surfaces which characterize the porous amorphous nature of the material as a result of chemical activation with KOH (Zhang et al., 2022b). The existence of the broad layers on the surface of CSAC implies that the surface is carved with curvature, suggesting a multiple pathway for AgNPs and TiO_2NPs loading (Chung et al., 2022). The elemental composition of CSAC presented Fig. 2g shows the abundance of carbon (89.85%) and oxygen (9.71 %), indicating the successful development of CSAC. The TEM images of CSAC@AgNPs@TiO_2NPs (Fig. 2d-e) show a good distribution of spherical AgNPs and TiO_2NPs on the surface of CSAC (Reçber et al., 2022). Additionally, there were some clusters in the dispersion of the NPs as can be seen in the TEM images of the CSAC@AgNPs@TiO_2NPs nanocomposite. The nanocomposite is composed mainly of carbon (52.30 %), oxygen (15.54 %), titanium (21.18%), silver (11.60%), and other elements as impurities (0.38 %) suggesting the successful loading of AgNPs and TiO_2NPs on the CSAC surface (Fig. 2h).

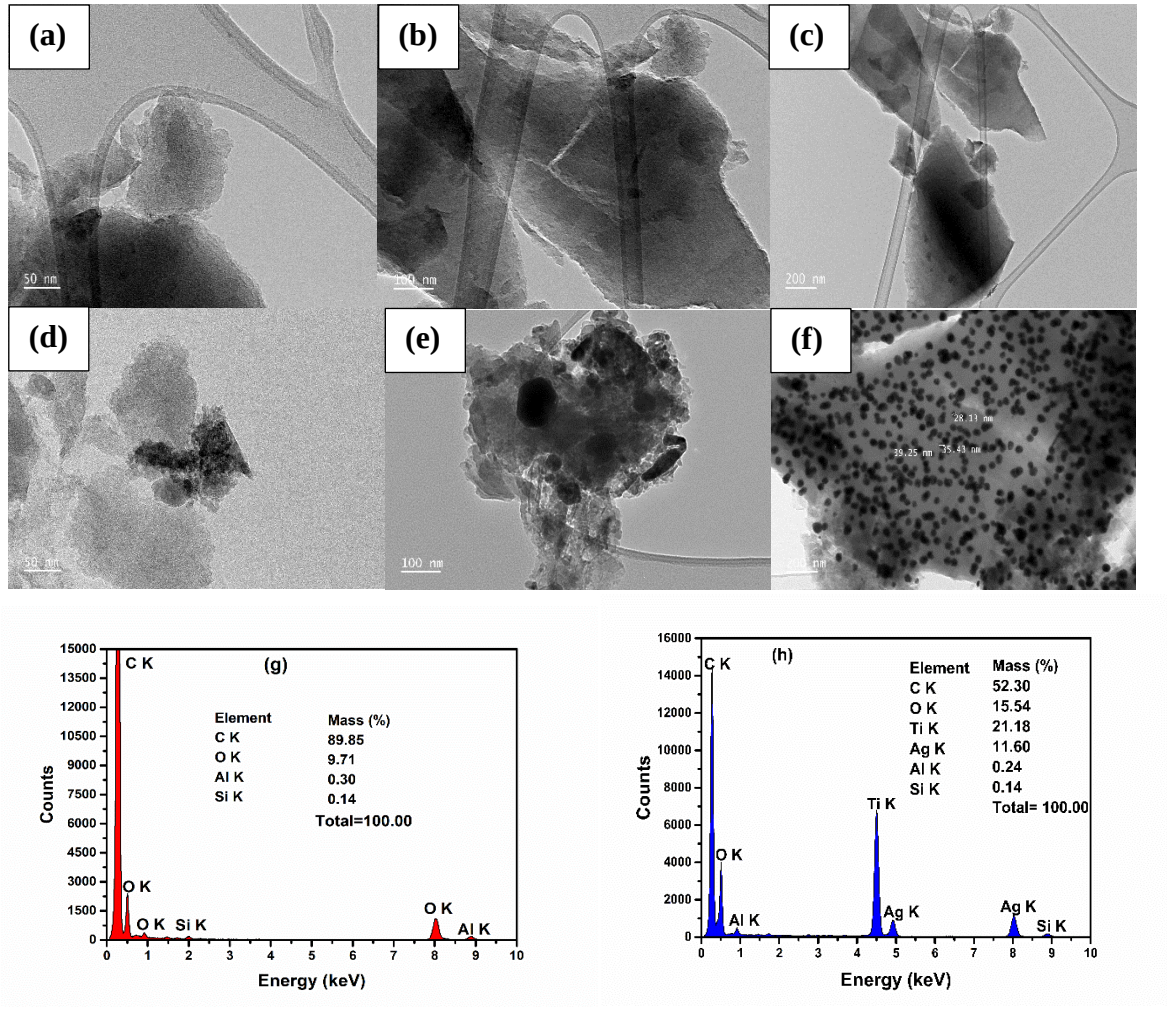

Fig. 2. TEM images for (a) CSAC, (b) CSAC@AgNPs@TiO_2NPs and EDS analysis for (g) CSAC, and (h) CSAC@AgNPs@TiO_2NPs

3.1.5. BET measurement

The BET surface area, Langmuir surface area, total pore volume, and average pore diameter of CSAC (Fig. S2(a)) were 310 m^2/g, 436 m^2/g, 0.134 cm^3/g, and 2.99 nm, respectively, while that of CSAC@AgNPs@TiO_2NPs (Fig. S2(b)) was reduced to 303 m^2/g, 381 m^2/g, 0.109 cm^3/g and 2.44 nm respectively. This may be attributed to the blockage of pores on the CSAC surface after loading TiO_2NPs and AgNPs. Furthermore, during biomass decomposition, alkyl groups and fatty acids were generated at higher temperatures leading to a higher surface area of CSAC (Yadav et al., 2022). The CSAC and CSAC@AgNPs@TiO_2NPs average pore sizes of 2.99 and 2.44 nm

revealed that they are majorly dominated by mesopores (2-50 nm). The mesopores in CSAC were formed mainly by volatile materials that escaped from the biomass under a high temperature conditions, thereby contributing to the high surface area of CSAC at high carbonization temperature (Liu et al., 2022A). In addition, the N_2 adsorption-desorption plots of CSAC and CSAC@AgNPs@TiO_2NPs demonstrated Type IV isotherm (mesopores) behaviours following the IUPAC classifications.

3.1.6. XPS analysis

The XPS analysis was conducted to evaluate the elemental composition and chemical state of the synthesized CSAC@AgNPs@TiO_2NPs (Fig. 3). The XPS spectrum shows the existence of Carbon, Oxygen, Nitogen, Silver, and Titanium, suggesting the successful anchoring of Ag and Ti on the CSAC surface (Fig. 3a). The N 1s peaks which were observed at 400.1 and 398.9 eV can be attributed to N-CH_3 and C=N-C bonds (Fig. 3b). The spectrum of the O 1s region, which is presented in Fig. 3c, shows characteristic peaks at 532.8 and 531.7 eV (Fig. 3c) which can be ascribed to OH groups in Ag-OH and Ti-OH as well as O in the Ti-O-Ti linkage of TiO_2 (Easwaran et al., 2022). The C 1s spectrum, which corresponds to C-atom bonds, is seen to have peaks at 288.9, 287.8, 286.3, and 284.8 eV corresponding to O-C=O, C=O, C-O, and C-C linkages (Fig. 3d). The Ag 3d high-resolution spectrum shows the presence of two peaks, 373.0 and 369.4 eV, which correspond to Ag $3d_{3/2}$ and Ag $3d_{5/2}$ core levels, respectively (Fig. 3e). The appearance of these peaks was a result of spin-orbital splitting thereby suggesting the formation of AgNPs in the CSAC@AgNPs@TiO_2NPs (Sharma et al., 2022b). The Ti 2p spectra (Fig. 3f) demonstrate two strong and sharp peaks at 463.0 and 457.4 eV, which relate to Ti $2p_{1/2}$ and Ti $2p_{3/2}$, suggesting that the main chemical state of Ti in the CSAC@AgNPs@TiO_2NPs nanocomposite was Ti^{4+} (Farrag, 2022).

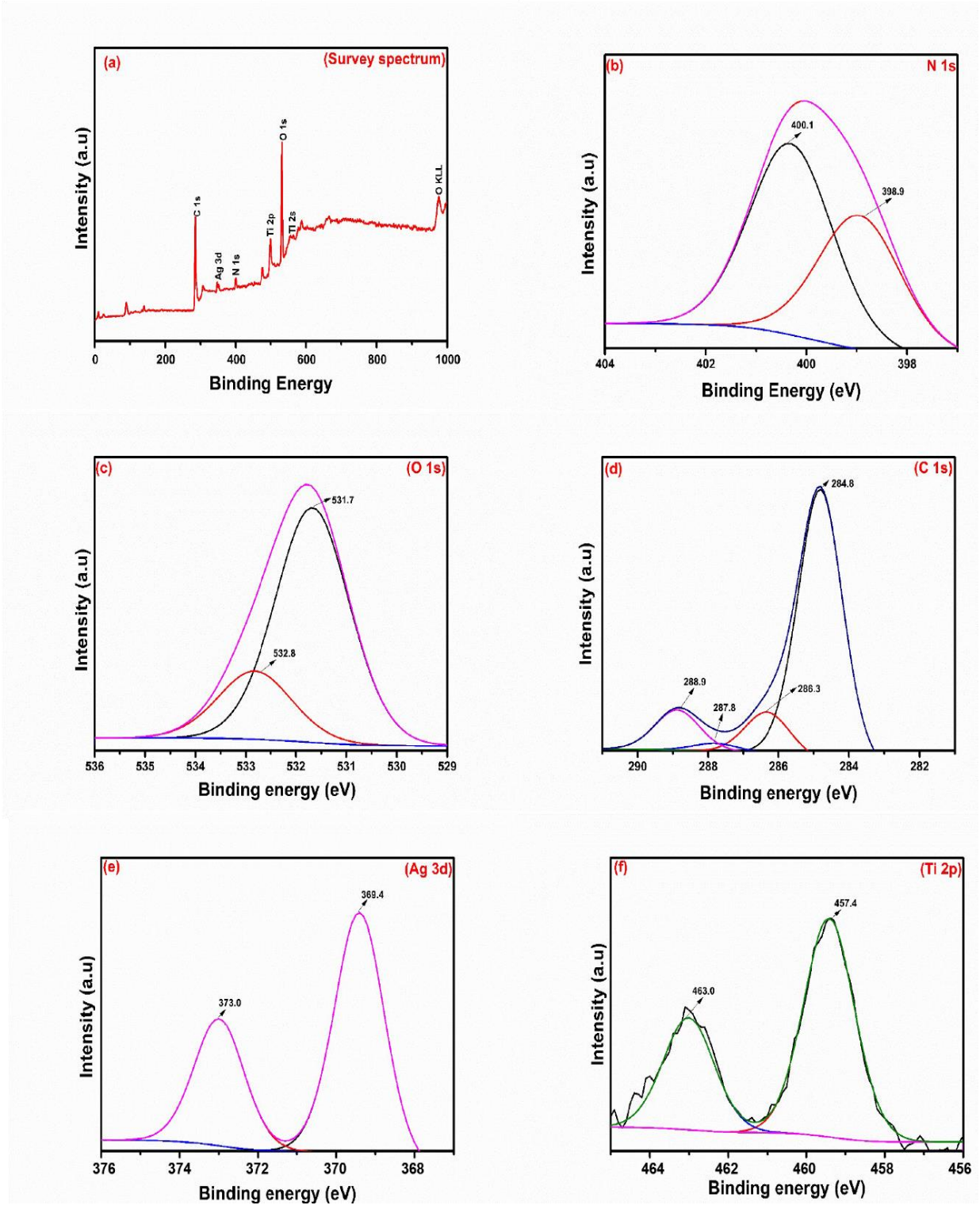

Fig. 3. XPS analysis for (a) survey spectrum, and deconvolution of spectra of (b) N 1s, (c) O 1s, (d) C 1s, (e) Ag 3d, and (f) Ti 2p for CSAC@AgNPs@TiO_2Nps nanocomposite.

311 3.2 Effect of adsorption parameters
312
313 The adsorption efficiency of CSAC@AgNPs@TiO_2NPs for MB removal was tested by varying
314 the initial concentration of MB (10-50 mg/L) and contact time (0-180 min) in batch studies, the
315 results for which are presented in Fig. S3(a). It can be seen in Fig. S3(a) that there was a
316 considerable increase in the percent adsorption of MB molecules for the five concentrations
317 investigated. This observation corresponds to excess active sites and resistance loss between the
318 adsorbent and adsorbent due to a high concentration gradient. As the adsorption time increases,
319 the adsorbent active sites gradually get saturated thereby resulting in a decrease in the adsorption
320 rate (Yara and Parlayici et al., 2022). Also, the removal rate of MB was seen to have decreased as
321 the initial concentration increased. It was also observed that equilibrium adsorption was attained
322 faster at lower MB concentration, i.e., initial concentration < 30 mg/L. At lower MB concentrations
323 of 10 and 20 mg/L, the percentage removal of MB onto CSAC@AgNPs@TiO_2NPs was 99.01 and
324 97.18 % and was attained at 10 and 15 min equilibrium time. At higher concentrations of 30, 40
325 and 50 mg/L, the efficiency removal was 94.01, 93.82 and 90.80% and it was achieved at 30 and
326 60 min respectively. This could be due to the availability of more active adsorption sites on the
327 CSAC@AgNPs@TiO_2NPs with less amount of MB molecules to occupy, so the limited available
328 MB molecules were adsorbed rapidly (Zhang et al., 2022a). It took more time to reach equilibrium
329 at higher MB concentrations because of the following: first, there were more adsorbate molecules
330 at fixed adsorbent dosage with few vacant sites, resulting in molecules queue formation waiting to
331 be adsorbed before adsorbent saturation; and second, the molecules had to go through a series of
332 adsorption processes, including the movement of molecules to the adsorbents' external surface
333 through a boundary layer, diffusion of molecules into the adsorbent pores, and diffusion of
334 adsorbates onto the adsorbent's interior pores (Obayomi et al., 2021; Thanh et al., 2022).

The percentage removal and adsorption capacity of MB onto CSAC@AgNPs@TiO_2NPs at pH range of 2-11 for 180 min is presented in Fig. S3(b). The plot (Fig. S3(b)) reveals that the highest removal and adsorption capacity (99.95% and 160 mg/g) was achieved at pH 10, while the least was attained at the lowest tested pH 2 (65% and 104.36 mg/g). This is because, at lower pH, the CSAC@AgNPs@TiO_2NPs surface becomes more positive due to the greater presence of hydrogen ions (protons) thereby promoting repulsion between the positively charged MB dye molecules and positively charged CSAC@AgNPs@TiO_2NPs resulting in removal and adsorption capacity decrease (Tran et al., 2022). However, as the pH of the solution increases, the hydrogen ions on the CSAC@AgNPs@TiO_2NPs surface become deprotonated thereby promoting electrostatic attraction between the positively charged MB dye molecules and negatively charged adsorbent (Ciftci, 2022). This observation was justified further using the pH_{pzc} as shown in Fig. S3(c). The plot (Fig. S3(c)) revealed that the pH_{pzc} of CSAC@AgNPs@TiO_2NPs was 8.6. Therefore, at pH $<pH_{pzc}$ the adsorbent surface will become more positively charged, and when the pH $>pH_{pzc}$, it becomes more negatively charged. However, the adsorption of MB dye molecules was greater at higher pH (9-11) because MB dye is a cationic dye and is more adsorbed at higher pH values (Liu et al., 2021). The influence of the solution pH on the removal of the MB dye molecule was observed to be involved in electrostatic interactions between the MB dye and adsorbent.

The effect of CSAC@AgNPs@TiO_2NPs dosage in the range of 10-80 mg on MB removal was investigated at equilibrium conditions and the results are provided in Fig. S3(d). It was evident from the Fig. S3(d) that the percentage removal and adsorption capacity of CSAC@AgNPs@TiO_2Nps improved from 84-99% and 135-159 mg/g with increasing the adsorbent dosage from 10-30 mg. This is because the availability of vacant sites increases on the surface of fabricated nanocomposite with an increase in the adsorbent dosage (Das et al., 2022).

However, there was no significant surge in the percentage removal and adsorption capacity when the adsorbent dosage was increased from 40-80 mg. This observation is due to the fact that at high adsorbent doses, coagulation tends to occur, resulting in a surface area reduction, thereby hindering the diffusion path for MB molecules (Subhan et al., 2022).

3.3. Adsorption kinetics

A greater comprehension of the rate and mechanism of MB adsorption onto CSAC@AgNPs@TiO_2NPs was investigated by fitting the equilibrium adsorption data to three kinetic models, namely; pseudo-first-order (PFO), pseudo-second-order (PSO), and Elovich models (Fig. S4(a-c)) as depicted in given equations

PFO: $q_t = q_e(1-\exp^{k_1 t})$ (4)

PSO: $q_t = \frac{q_e^2 k_2 t}{1+q_e k_2 t}$ (5)

Elovich: $q_t = \frac{1}{\beta}\ell nt + \frac{1}{\beta}\ell n(\alpha\beta)$ (6)

The adsorption kinetic parameters, regression coefficients (R^2), and their error functions for the models tested are presented in Table 1. A close and careful observation of the evaluated parameters revealed that the adsorption of MB onto CSAC@AgNPs@TiO_2NPs was best described by PSO compared to PFO and Elovich model with the following reasons; the higher adsorption rate (k_2= 0.284 g/mg/min, h_2 = 2845 mg/g/min) from PSO constituted evidence of a rapid absorption process; also, increase in the initial rate at the initial MB concentration could be attributed to the build-up of competition at the start of the adsorption process and the availability of the active sites (Wang et al., 2018), hence, as the concentration increases, the competition for the active site also increases, thereby leading to a decrease in the rate constant (k_2) values (Joshiba et al., 2021); the

regression coefficient (R^2) values of PSO was closer to unity when compared to other models; finally, the experimental q_e values were very close to the calculated q_e, values which further supports the best fitting of PSO (Çiftçi, 2022). In order to further validate the best fitness of PSO to kinetic data, the models were further subjected to error analysis such as Sum of Square error (SSE), Non-linear Chi-square (χ^2), Hybrid fractional error function (HYBRD) and Derivative of Marquardt's percent standard deviation (MPSD). It was observed from the tabulated results the SSE, χ^2, HYBRID and MPSD values for PSO were smaller across all the concentrations when compared to other models. According to studies, the kinetic model that describes the adsorption kinetic process is more accurate the lower the statistical validity model values (Chen et al., 2022).

Table 1: Sorption of MB onto CSAC/AgNPs/TiO_2NPs nanocomposite kinetic model parameters

Kinetics Model parameters	10 mg/L	20 mg/L	30 mg/L	40 mg/L	50 mg/L
Pseudo-first-order					
$q_{e,\ exp}$ (mg/g)	29.400	62.270	87.400	121.830	145.470
$q_{e,\ cal}$ (mg/g)	31.193	68.0104	97.839	138.645	168.479
$k_1(min^{-1})$	0.0174	0.00518	0.00224	0.00108	0.000979
h_1 (mg/g/min)	0.543	0.352	0.219	0.150	0.165
R^2	0.972	0.954	0.944	0.979	0.950
SSE	3.216	32.952	108.966	282.754	529.428
χ^2	0.103	0.485	1.114	2.0394	3.142
HYBDRID	0.109	0.529	1.247	2.321	3.639
MPSD	0.00372	0.00850	0.0143	0.0191	0.0250
Pseudo-second-order					
$q_{e,\ exp}$ (mg/g)	29.400	62.270	87.400	121.830	145.470
$q_{e,\ cal}$ (mg/g)	29.777	63.928	90.512	125.781	153.296
k_2(g/mg/min)	0.284	0.213	0.158	0.111	0.121
h_2 (mg/g/min)	251.547	871.306	1296.0412	1748.213	2845.806
R^2	0.999	0.990	0.989	0.999	0.991
SSE	0.142	2.749	9.685	15.613	61.245
χ^2	0.00477	0.0430	0.107	0.124	0.400
HYBDRID	0.00483	0.0441	0.111	0.128	0.421
MPSD	0.000164	0.000709	0.00127	0.00105	0.00289

Elovich					
α(g.min^2/mg)	93.00290	95.798	70.318	53.253	72.647
β(g.min/mg)	0.241	0.100	0.0635	0.0409	0.0342
R^2	0.583	0.667	0.743	0.871	0.811
SSE	0.219	1.146	0.412	266.481	0.362
χ^2	0.00733	0.0181	0.00468	1.929	0.00248
HYBDRID	0.00745	0.0184	0.00471	2.187	0.00249
MPSD	0.000253	0.000295	0.0000539	0.0180	0.0000171

The Elovich model (Fig S4(c)) was employed to calculate the α and β values by the slope and intercept of qt vs ln (t) plot. The values of α (adsorption rate) (Table 1) increase as the initial concentration increases as a result of the availability of more active at the instance of the adsorption process. The values 1/β at different initial concentrations (10-50 mg/L) were evaluated as 4.146, 1.499, 1.347, 1.148 and 1.233, respectively. The values of 1/β reflect the available sites of adsorption. The observable decrease in the sites as the concentration increases suggested the occupancy of the active sites as the MB adsorbate increases, hence a low value of 1/β indicates pore-filling and saturation of the vacant site.

3.4. Intra-particle diffusion (IPD) model

To ascertain whether intra-particle diffusion, boundary layer diffusion, or both govern the adsorption of MB dye molecules onto CSAC@AgNPs@TiO2NPs, the (IPD) model was employed. The intra-particle diffusion model (IPD) equation is given by;

Intra-particle diffusion: $$q_t = k_{IPD} t^{1/2} + C \quad (7)$$

where k_{IPD} is the IPD rate constant (mg/gmin$^{1/2}$). The plot of q_t vs $t^{1/2}$ which was presented in Fig. S4(d) revealed a multi-layer plot, suggesting that the adsorption of MB onto CSAC/AgNPs/TiO_2 NPs nanocomposite was controlled by two steps. The slope and the intercept of the plot presented

406 in Fig. S4(d), were employed to evaluate the values of the rate constant ($k_{IPD,1}$ and $k_{IPD,2}$) and the
407 boundary layer thickness (C) for the curve (boundary layer diffusion) and linear (intra-particle
408 diffusion) area of the plot. The result findings as shown in Table S1 revealed that the boundary
409 thickness, C values for both boundary layer region (11.058 to 61.067) and intra-particle diffusion
410 section (28.805 to 146.886) increase as the MB dye initial concentrations increases from 10-50
411 mg/L. This can be understood if one considers the fact that as the thickness of the boundary layer
412 increases, the probability of internal mass transfer rises, whereas the probability of external mass
413 transfer falls (Liu et al., 2022b). Furthermore, the intra-particle diffusion rate constant ($k_{IPD,2}$)
414 values when compared with that of the boundary layer diffusion (k_{i1}) was lower, suggesting that
415 the MB dye adsorption onto CSAC@AgNPs@TiO_2NPs was governed by intra-particle diffusion.
416 This assertion is further supported by the fact that the intra-particle diffusion R^2 values (closer to
417 1) when compared to the boundary layer diffusion R^2 values (Leyva-Ramos et al., 2021).

418
419 3.5. Adsorption isotherms
420
421 In order to study the interaction between the adsorbent and adsorbate molecule in an adsorption
422 media, the adsorption isotherm models are widely employed (Sharma et al., 2022a). In this study,
423 Langmuir, Freundlich, Temkin, Sips, and Toth models were used to fits the adsorption equilibrium
424 data of MB adsorption on CSAC@AgNPs@TiO_2NPs.
425 Langmuir isotherm model predicts that adsorbent surfaces have homogeneous binding sites with
426 identical adsorption energies with no adsorption taking place at the adsorbed sites; therefore, the
427 adsorption can be classified as monolayer adsorption (Langmuir, 1916). The Langmuir model's
428 non-linear equation can be expressed as follows.

$$q_e = \frac{q_{max} K_L C_e}{1 + K_L C_e} \quad (8)$$

where q_{max} (mg/g), K_L (L/g) are the maximum adsorption capacity and Langmuir's model constant, respectively.

Freundlich isotherm model assumes the heterogeneity of the adsorbent surfaces (multilayer) (Freundlich, 1906). The non-linear Freundlich model can be described as follows:

$$q_e = K_F C_e^{\frac{1}{n}} \quad (9)$$

where, K_F and n is the Freundlich adsorption capacity and the heterogeneity factor, respectively. The value of n depicts the nature of adsorption. The adsorption is considered irreversible when the value of 1/n = 0. Likewise, the adsorption is assumed favourable when the value of 1/n lies between 0 and 1. The value of n less than unity predicts that the process adsorption is unfavourable.

The Temkin isotherm model predicts that the adsorption heat decreases linearly for all molecules rather than logarithmically. Additionally, the Temkin model predicts that the binding energy is evenly distributed and that the surface coverage increases as a result of adsorbate-adsorbent interactions (Tempkin and Pyzhev. 1904). The Temkin model in its non-linear form is expressed as.

$$q_e = B \ln(A_T C_e) \quad (10)$$

where, B (J/mol) signifies the adsorption heat energy, and A_T (L/g) is the maximum binding energy relating to the equilibrium binding constant.

The Sips model is a hybrid model formed by the mixture of Langmuir and Freundlich models. In homogeneous and heterogeneous systems, the Sips model can be employed to predict accurately monolayer adsorption (Sips, 1948). The non-linear equation is represented as.

$$q_e = \frac{q_{ms} K_S C_e^{ns}}{1 + K_S C_e^{ns}} \quad (11)$$

where, q_{ms} correspond to the adsorption capacity (mg/g), K_S is the constant associated with the Sips isotherm model, and $and\ ns$ is the exponent of the Sips isotherm model. Homogeneous adsorption occurs when the ns value is ≥1 while heterogeneous adsorption takes place when the ns value is < 1.

The Toth isotherm model assumes the adsorption heterogeneous systems that meet the low- and high-end limits of adsorbate concentration (Toth, 1971). The non-linear empirical model of the Toth model is given by;

$$q_t = \frac{q_{mT} C_e}{(a_T + C_e^z)^{1/z}} \quad (12)$$

where q_{mT} is the adsorption capacity (mg/g), a_T is the Toth constant (mg/L), and z is the adsorbent surface heterogeneity. The value of z ≥1 denotes the transformation of the Toth isotherm equation into the Langmuir equation showing that homogeneous adsorption has occurred. The value of z <1 indicates surface heterogeneity with strong adsorbent-adsorbate interactions.

The adsorption isotherm fitting plots and relevant parameters for Langmuir, Freundlich, Temkin, Sips, and Toth models are depicted in Fig. S5(a-c) and Table 2. The regression coefficient (R^2), Sum of Square error (SSE), Non-linear Chi-square (χ^2), Hybrid fractional error function (HYBRD) and Derivative of Marquardt's per cent standard deviation (MPSD) were employed to compare the fitting accuracy of the two (Langmuir, Freundlich, and Temkin) and three (Sips and Toth) parameter models studied.

Based on the comparison, the adsorption of MB dye onto CSAC@AgNPs@TiO_2NPs experimental data fitted well to the Sips isotherm model with higher regression coefficient (>0.996) and lowest SSE, χ^2, HYBRID, and MPSD values. The Sips model exponent (ns) values

at a different temperature greater than 1, suggests that the adsorption of MB dye was occupied on the homogeneous surface (monolayer adsorption) of CSAC@AgNPs@TiO_2NPs nanocomposite. Aside, from the Sips model, the Langmuir, and Toth (Z >1) models also fitted well to the adsorption equilibrium data with R^2 values closer to 1 and the lowest error values verifying the monolayer adsorption mechanism. Along with the Sips model, the Langmuir and Toth models also fitted well the MB dye adsorption based on the higher R^2 and lower error values verifying the monolayer adsorption mechanism of MB dye onto CSAC@AgNPs@TiO_2NPs nanocomposite.

The maximum adsorption capacity calculated at 303, 313 and 323 K were 177.4, 180.6, and 184.3 mg/g respectively. The adsorption of MB dye onto CSAC@AgNPs@TiO_2NPs nanocomposite degree of fitness follows the pattern: Sips (best fit) > Langmuir > Toth >Temkin > Freundlich.

Table 2. Isotherm models parameters MB dye adsorption on CSAC@AgNPs@TiO_2NPs

Isotherm models	Parameters	Temperature (K)		
		303	313	323
Langmuir	q_{max} (mg/g)	144.496	148.258	156.797
	KL (L/g)	1.245	5.054	1.804
	R^2	0.985	0.990	0.994
	SSE	4.561	6.011	5.101
	χ^2	55.698	26.784	32.016
	HYBDRID	0.113	0.567	0.634
	MPSD	0.00671	0.00981	0.00934
Freundlich	K_F	74.415	108.325	88.716
	1/n	0.278	0.271	0.332
	R^2	0.768	0.939	0.944
	SSE	20.313	19.567	22.091
	χ^2	395.546	135.755	116.881
	HYBDRID	2.116	8.567	11.567
	MPSD	0.163	0.432	0.105
Temkin	B (J/mol)	27.429	25.230	29.932
	K_T (L/g)	16.677	97.857	25.420
	R^2	0.897	0.990	0.991
	SSE	15.456	17.661	12.011
	χ^2	175.319	31.575	47.925

	HYBDRID	0.934	1.340	2.111
	MPSD	0.0461	0.0716	0.0908
Sips	q_{ms}	177.439	180.645	184.304
	Ks	1.446	1.766	1.168
	ns	1.210	1.629	1.770
	R^2	0.998	0.997	0.998
	SSE	2.311	1.886	3.0310
	χ^2	18.317	20.904	13.096
	HYBDRID	0.103	0.432	0.5120
	MPSD	0.00121	0.00630	0.00203
Toth	q_{mT}	191.717	148.700	145.901
	a_T	1.574	2.452	0.359
	z	1.210	1.728	1.877
	R^2	0.985	0.989	0.993
	SSE	7.107	9.056	5.891
	χ^2	89.205	29.634	38.978
	HYBDRID	0.670	0.813	1.103
	MPSD	0.0162	0.0160	0.00991

485
486

487 3.6. Thermodynamics evaluation

488 Thermodynamic studies of the adsorption of MB dye onto CSAC@AgNPs@TiO_2NPs were
489 investigated at 303 K, 318 K and 318 K. The enthalpy (ΔH), entropy (ΔS) and Gibbs free (ΔG)
490 were calculated using Vant'Hoff, Gibb's free energy and Arrhenius models as presented in
491 equations 13 – 16 (Pi et al., 2018; Wishal et al., 2022).

492 $K_D = qe/Ce$ (13)

493 Van't Hoff: $\ln K_D = \frac{\Delta S}{R} - \frac{\Delta H}{RT}$ (14)

494 Arrhenius: $\ln k_L = \ln A - \frac{Ea}{RT}$ (15)

495 Gibbs Free Energy $\Delta G° = \Delta H - T\Delta S$ (16)

496 where k_L is the constant of the Langmuir isotherm model and A is the Arrhenius constant. Fig
497 S5(d). shows Van't Hoff linear plot of $\ln K_D$ against the reciprocal of temperature (1/T). At various

concentrations (10 – 50 mg/L), the thermodynamics studies were carried out and advantageous, the values of the regression coefficient (R^2) and residual sum of squares (RSS) as presented in Table S2 show that Van't Hoff model is well fitted to the thermodynamics data. The results exhibit that the values of enthalpy change ranging are positive indicating that the adsorption of MB dye solution was endothermic in nature which is an indication that the equilibrium constant increases at higher temperatures (Dada et al., 2017). The endothermic nature is further supported by the positive values of the Activation energy (E_a=16.128 kJ $mol^{-1}K^{-1}$) as depicted in Fig. S6. The positive values of ΔS suggested good randomness and equilibration of the solid-liquid interface of CSAC@AgNPs@TiO_2NPs -MB system. The negative values of the $\Delta G°$ are essentially proof of the feasibility and spontaneity of the adsorption process (Gupta and Nayak, 2012; Mpatani et al., 2020; Obayomi et al., 2021) (Mpatani et al., 2020; Gupta and Nayak, 2012; Dada et al., 2015). It is suggested that the endothermic nature of this process is an advantage because CSAC@AgNPs@TiO_2NPs will find relevance in industries. It is well known that most industrial effluents are always discharged hot. Hence, there will not be a need to open the pores in the nano-adsorbent by heating before utilizing it for waste treatment since its adsorptive route is endothermic in nature. The activation energy (E_a) and enthalpy (ΔH) values are less than 40 kJ/mol, and the adsorption process is dominated by physical adsorption.

3.7 Competing ions influence on MB removal

The water system is always polluted with either alkali or alkaline earth metal ions. These co-existing ions increase the salinity and background electrolyte of the water body (Dada et al., 2017). In this study, the influence of competing ions (anions and cations) on MB removal was conducted at optimal conditions (pH =10, contact time =60 min, initial MB concentration= 50 mg/L, temperature = 323 K and dosage =30 mg) using 0.01 M concentration of calcium chloride ($CaCl_2$),

sodium chloride (NaCl), sodium bicarbonate ($NaHCO_3$), and sodium nitrate ($NaNO_3$) ionic salts. Some co-existing ions with excellent chemical reactivity and strong complexation potentials towards the adsorbate and adsorbent surface may have an abrupt impact on the movement, transformation, and bioavailability performance of pollutants in the environmental medium. The experimental plot revealed that the percentage removal of MB was reduced in the presence of competing ions, which may have occupied the adsorbent active sites and impeded the bond formation between the adsorbate and adsorbent. As observed from the plot (Fig. S7(a)), the results also showed that the removal of MB was more affected significantly by the presence of Ca2+ and Na+. The presence of the competing ions influences the activity coefficient of the adsorbates (dye, polymeric species or heavy metal ions) which resultantly limits the mass transfer and removal efficiency as a result of electrostatic competitions for the available sites (Gang et al., 2012; Soleymanzadeh et al., 2015). This could also be explained based on the higher chemical valence state and smaller ionic radius. The higher removal of MB in the presence of Ca^{2+} and Na^{+} could also be attributed to the fact that the Ca^{2+} and Na^{+} in an aqueous medium release positive ions after dissolution, and CSAC@AgNPs@TiO_2Nps surface is negatively charged (pH_{pzc}= 8.6), hence resulting in electrostatic attraction arising from a compressed electrical diffuse double layer (Yadav et al., 2022). The effect on the removal efficiency could be due to electrostatic repulsion that takes place between the negative charge NO_3^-, and HCO_3^- and negatively charge CSAC@AgNPs@TiO_2Nps surface. In overall, the percentage removal of MB was observed to follow this order: $Ca^{2+} > Na^{+} > NO_3^- > HCO_3^-$.

The significant decrease in MB removal efficiency in the presence of HCO_3^- can be attributed to the coordinated action of strongly competitive adsorption and vigorous radical scavenging. However, specific H+ and OH^- ions may be adsorbed readily to some extent by HCO_3^-.

3.8 Reusability studies

The CSAC@AgNPs@TiO_2NPs regeneration studies were performed by washing after MB adsorption with ethanol mixed with acetic acid and then washed with ultrapure water several times before being dried and reused. This is to ensure that the MB dye is completely removed from the adsorbent materials. After regeneration, 50 mg of the spent CSAC@AgNPs@TiO_2NPs was measured and transferred into a 250 mL flask containing 100 mL (50 mg/L) of the MB dye solution. The flasks were placed in a shaker incubator at a shaker speed of 140 rpm under equilibrium conditions of temperature 50 ^oC and pH=10 for 60 min. The adsorption-desorption experiments of MB onto CSAC@AgNPs@TiO_2NPs were subjected to six consecutive cycles and the result is presented in Fig. S7(b). The result shows that the removal efficiency of MB dye onto CSAC@AgNPs@TiO_2Nps was 99.33% in the first cycle but went on decreasing to 86.97 % at the end of the sixth cycle due to surface area decrease and active sites saturation on the surface of the CSAC@AgNPs@TiO_2Nps. Therefore, the deduction of about 1% removal between the fifth and sixth cycle suggests that the nanocomposite is active, effective and showed good regeneration stability even after six cycles.

3.9 Application of CSAC@AgNPs@TiO_2Nps in natural water

The removal of MB in real water was tested by dissolving MB solution containing 10 mg/L of MB in deionized water, tap water, borehole water and rainwater at optimal conditions. The CSAC@AgNPs@TiO_2NPs nanocomposite was observed (Fig. S7(c)) to have exhibited excellent adsorptive performance with MB in real water, suggesting that the nanocomposite had a good potential and effective for the uptake of MB in real water application with removal efficiency of above 97%.

568 3.10 Comparative study

569 The adsorption performance of CSAC@AgNPs@TiO_2NPs nanocomposite was compared with
570 other previous studies reported in the literature for MB dye treatment (Table 3). This was to
571 establish the advantages and the adsorptive performance of CSAC@AgNPs@TiO_2NPs. The
572 adsorption capacity of the proposed material was superior to that reported in previous studies,
573 implying that the synthesized nanomaterial can be employed effectively for MB dye treatment
574 from aqueous environments.

575 Table 3. Comparison of MB dye maximum adsorption capacity (q_{max}) onto different adsorbents

Adsorbents	Equilibrium conditions	q_{max} (mg/g)	References
Sulphonated hawthorn kernel (SHK)	pH 10, 3600 min, 298 K	151.5	Akköz et al., (2019)
Oxone treated hydrochar (OHC)	pH 7, 240 min, 318 K	86.7	Madduri et al., (2020)
CS/AAm/IA/GO	pH 8, 90 min, 298 K	247.5	Tamer et al., (2022)
Cu-BDC-NH_2	pH 7, 60 min, 328 K	95.14	Pamei et al, (2022)
FeMn-HNTs-4	pH 7, 120 min, 303 K	96.5	Zhang et al., (2023)
Magnesium ferrite spinel ($MgFe_2O_4$)	pH 11, 120 min, 298 K	78.1	Ivanets et al., (2022)
Agar/GO/ZnO	pH 6.5, 40 min, 293 K	33.3	Moradi et al., (2022)
Cellulose–chitosan composite beads	pH 6, 90 min, 293 K	55.0	Al-Ghamdi, (2022)
Magnetic biochar	pH 6.7, 120 min, 298 K	186.0	Zheng et al., 2022
CSAC@AgNPs@TiO_2NPs	pH 10, 60 min, 323 K	186.3	This study

576

577 3.11 Mechanism of adsorption

578 The plausible adsorption mechanism of MB adsorption onto CSAC@AgNPs@TiO_2NPs is
579 presented in Fig. 4. The adsorption mechanisms are described in terms of adsorbent textural,
580 functional, structural, crystalline properties (BET, FTIR, SEM and XRD) as well as the
581 electrostatic forces (pH), and MB properties in aqueous solution. Adsorption procedures may
582 result from intraparticle film transport, bulk transfer and MB adsorption on the nanocomposite.

The BET surface area of CSAC@AgNPs@TiO_2NPs was observed to have played an important role in promoting the adsorption of MB as this is evident by the presence of mesopores on the synthesized nanocomposite material. The BET surface area and total pore volume of CSAC@AgNPs@TiO_2NPs nanocomposite before MB dye adsorption was measured to be 318 m^2/g and 0.109 cm^3/g while after adsorption it was noted to be 289 m^2/g and 0.00369 cm^3/g. The surface area and pore volume reduction after MB dye adsorption suggest a pore filling as a result of the dye molecule occupation after adsorption. The SEM analysis before and after MB adsorption onto CSAC@AgNPs@TiO_2Nps as depicted in Fig. 4 (a-b) when compared showed a rough surface covering after MB adsorption. However, the morphological structure showed no signs of deterioration, suggesting that the adsorbent can be regenerated and reused and the adsorption process may be triggered by physical force.

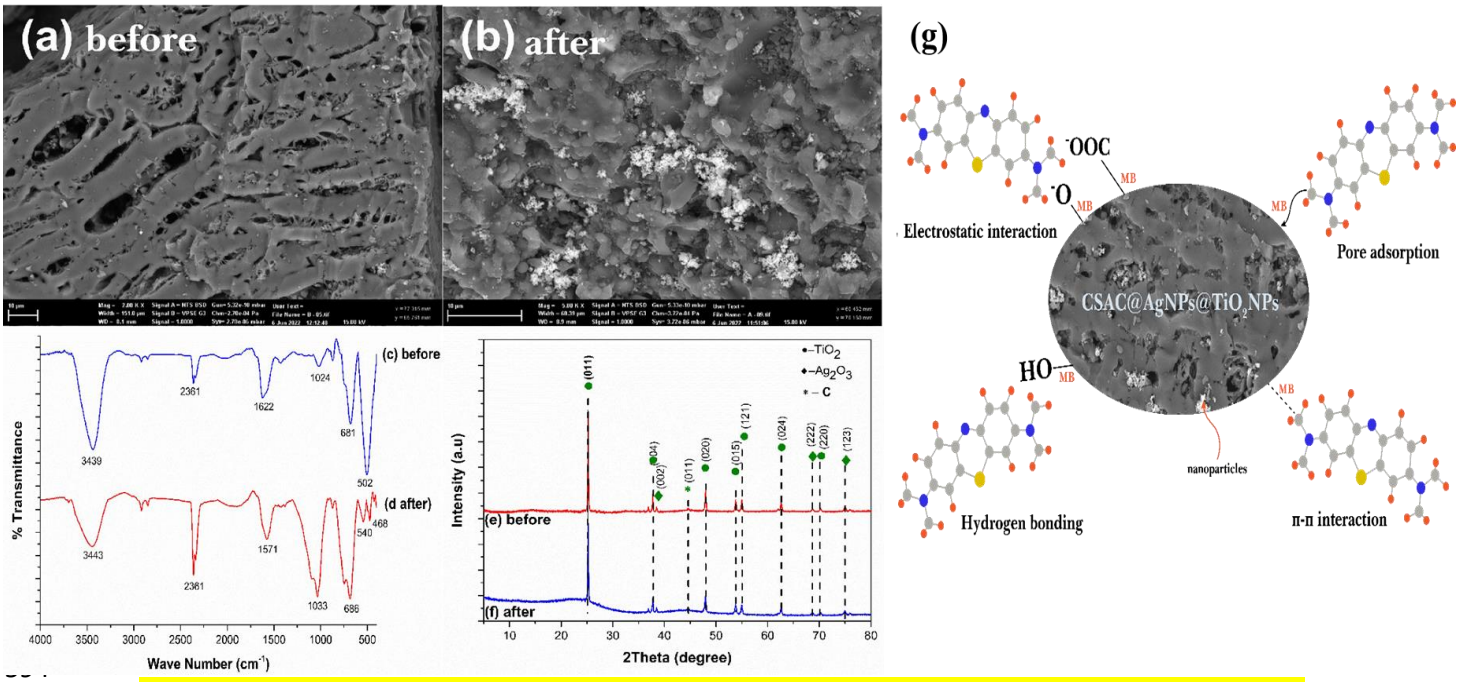

Fig. 4. (a-b) SEM micrograph (c-d) FTIR analysis, and (e-f) XRD analysis before and after adsorption of MB on CSAC@AgNPs@TiO_2Nps nanocomposite (g) The proposed schematic adsorption mechanism insights of MB on CSAC@AgNPs@TiO_2NPs

The FTIR spectra of CSAC@AgNPs@TiO_2Nps nanocomposite before and after MB adsorption are presented in Fig. 4(c-d). The results of CSAC@AgNPs@TiO_2Nps before adsorption (Fig. 4c) have peaks at 3443, 2361, 1622, and 1024 which were attributed to -OH stretching, vibrational stretching of -C=O, aromatic C=C vibrations, and C-O. In comparison with after adsorption spectra (Fig. 4d) it can be observed that peaks for the -OH stretching and C-O relocated (slight increase) from 3439 to 3443 cm^{-1} and 1024 to 1033 cm^{-1}. Also, a slight decrease in the peak was observed for aromatic C=C vibrations from 1622 to 1571 cm^{-1}. The peak for the vibrational stretching of -C=O was observed to remain unchanged after adsorption. In addition, some peaks were observed to have disappeared while new peaks were formed. Furthermore, the two peaks suggesting the presence of AgNPs (502 cm^{-1}), and TiO_2NPs (681 cm^{-1}) were also observed to have increased to 540 and 686 cm^{-1} respectively. The disappearance, formation and slight peak shift after adsorption could be attributed to interactions between the MB dye and CSAC@AgNPs@TiO_2NPs surface.

The XRD MB dye adsorption before and after onto CSAC@AgNPs@TiO_2NPs can be seen in Fig. 4 (e-f). It was observed from the result that there was no noticeable change in the crystal planes of CSAC@AgNPs@TiO_2Nps nanocomposite before and after adsorption, signifying that there was no damage in the crystal structure during the MB treatment. This observation established the fact that the adsorption process is driven by a physical adsorption mechanism. The solution pH plays an important role in determining the CSAC@AgNPs@TiO_2NPs surface charge. The pH_{pzc} value evaluated (8.6) revealed a negatively charged surface of CSAC@AgNPs@TiO_2Nps. However, at pH >pHpzc the adsorbent surface becomes more negatively charged thereby facilitating electrostatic attraction between the positively charged MB dye molecules. Furthermore, electrostatic repulsion was observed between the positively charged MB dye molecules and positively charged adsorbent surface at pH <pHpzc. Thus, it can be suggested that

electrostatic attraction is one of the driving forces for the interaction between CSAC@AgNPs@TiO_2Nps and MB dye molecules. Thus, the MB dye adsorption onto CSAC@AgNPs@TiO_2Nps is governed by electrostatic attraction, pore-adsorption, hydrogen bonding, and π-π interaction (see Fig. 4g).

3.12 CSAC@AgNPs@TiO_2NPs separation and disposal

After the adsorption studies of MB on CSAC@AgNPs@TiO_2NPs, the suspensions were collected and filtered by vacuum filtration with the aid of a PVDF membrane of 0.45 µm to separate from the liquid waste. After separation, the nanocomposite was collected by a licensed professional in accordance with local standards for solid waste disposal.

4. Conclusions

In this study, the decoration of AgNPs and TiO_2 NPs on CS-derived AC (CSAC@AgNPs@TiO_2NPs) was successfully synthesized. The fabricated adsorbent's morphological, crystallinity, textural, functional, surface charge, size distribution, elemental composition, and surface chemical properties were characterized. Results, most especially from TEM-EDX, SEM, and XPS analysis, confirmed that nanoparticles were evenly distributed on the CSAC surface with a BET surface area of 301 m^2/g. Batch adsorption studies showed that the adsorption can be highly influenced by the amount of adsorbent dose, contact time, pH, initial concentration and the temperature. The isotherm analysis exhibited that the Sips model best described the adsorption process with a maximum adsorption capacity of 184 mg/g, suggesting the adsorption of MB on the CSAC@AgNPs@TiO_2NPs is a monolayer adsorption. Among the PFO and PSO kinetic model, the adsorption kinetics were best explained by PSO model, implying a chemical adsorption is the rate limiting step in the adsorption of MB on CSAC@AgNPs@TiO_2NPs. The thermodynamics study revealed that the adsorption process is

endothermic, and spontaneous with increase in the degree of freedom between the adsorbate and adsorbent. Furthermore, the adsorption-desorption cycle showed a good percentage removal of MB dye (>85 %) from aqueous environment after 6 cycles. The prepared CSAC@AgNPs@TiO_2 nanocomposite showed an excellent applicability in aqueous media. In conclusion, the synthesized CSAC@AgNPs@TiO_2NPs nanocomposite has demonstrated to be potentially effective adsorbent for the remediation of MB dye molecules from aqueous environments and therefore can be used as a promising adsorbent for the industrial waste water.

Acknowledgements

The authors acknowledged Curtin Malaysia Postgraduate Research Scholarship (CMPRS), Curtin University, Malaysia for the financial assistance. We also appreciate Global Centre for Environmental Remediation (GCER)'s laboratory and EMX unit, The University of Newcastle, Australia and the Surface Analysis Laboratory, MWAC, located at the University of New South Wales, Australia for instrumental support. The authors also appreciated the immense contribution of Alisa Makarova, BSc. (Biot) for her editorial and technical input.

References

Ahmed, S. F., Mofijur, M., Nuzhat, S., Chowdhury, A. T., Rafa, N., Uddin, M. A., Inayat, A., Mahlia, T. M. I., Ong, H. C., Chia, W. Y., Show, P. L., 2021. Recent developments in physical, biological, chemical, and hybrid treatment techniques for removing emerging contaminants from wastewater, Journal of Hazardous Material, 416, 125912.

Ahmad, R., Ansari, K., 2022. Fabrication of alginate@silver nanoparticles (Alg@AgNPs) bionanocomposite for the sequestration of crystal violet dye from aqueous solution, International Journal of Biological Macromolecules, 218, 157-167.

Akköz, Y., Coşkun, R., Delibaş, A., 2019. Preparation and characterization of sulphonated bio-adsorbent from waste hawthorn kernel for dye (MB) removal Journal of Molecular Liquids, 287, 110988.

Al-Ghamdi, Y. O., 2022. Immobilization of cellulose extracted from *Robinia Pseudoacacia* seed fibers onto chitosan: Chemical characterization and study of methylene blue removal, Arabian Journal of Chemistry, 15,104066.

Ali, Rizwan, Zaheer Aslam, Reyad A. Shawabkeh, Anam Asghar, and Ibnelwaleed A. Hussein.

2020. “BET, FTIR, and RAMAN Characterizations of Activated Carbon from Waste Oil Fly Ash.” Turkish Journal of Chemistry 44, 279.

Bathula, C., Rabani, I., Sekar, S., Youi, H-K., Choy, J-Y., Kadam, A., Shretha, N. K., Seo, Y-S., Kim, H-S., 2021. Enhanced removal of organic dye by activated carbon decorated TiO_2 nanoparticles from *Mentha Aquatica* leaves via ultrasonic approach, Ceramics International, 47, 8732-8739.

Boughrara, L., Zaoui, F., Guezzoul, M., Sebba, F. Z., Bounaceur, B., Kada, S. O., 2022. New alginic acid derivatives ester for methylene blue dye adsorption: kinetic, isotherm, thermodynamic, and mechanism study, International Journal of Biological Macromolecules, 205, 651-663.

Chen, X., Hossain, M. F., Duan, C., Lu, J., Tsang, Y. F., Islam, M. S., Zhou, Y. 2022. Isotherm models for adsorption of heavy metals from water - A review, Chemosphere, 307, 135545.

Chung, J., Sharma, N., Kim, M., Yun, K., 2022. Activated carbon derived from sucrose and melamine as low-cost adsorbent with fast adsorption rate for removal of methylene blue in wastewaters, Journal of Water Process Engineering, 47, 102763.

Ciftci, H., 2022. Removal of methylene blue from water by ultrasound-assisted adsorption using low-cost bentonites, Chemical Physics Letters, 802, 139758.

Dada, A. O., Adekola, F. A., Odebunmi, E. O., 2017a. Liquid phase scavenging of Cd (II) and Cu (II) ions onto novel nanoscale zerovalent manganese (nZVMn): Equilibrium, kinetic and thermodynamic studies, 2017. Environmental Nanotechnology, Monitoring & Management, 8, 63-72.

Das, L., Das, P, Bhowal, A., Bhattacharjee, C., 2020. Synthesis of hybrid hydrogel nano-polymer composite using graphene oxide, chitosan, and PVA in its application in wastewater treatment, Environmental Technology and Innovation, 18, 100664.

Durrani, W. Z., Nasrullah, A., Khan, A. S., Fagieh, T. M., Bakhsh, E. M., Akhtar, K., Khan, S. B., Din, I. U., Khan, M. A., Bokhari, A., 2022. Adsorption efficiency of date palm based activated carbon-alginate membrane for methylene blue, Chemosphere, 302, 134793.

Easwaran, G., Packialakshmi, J. S., Syed, A., Elgorban, A. M., Vijayan, M., Sivakumar, K., Bhuvaneswari, K., Palanisamy, G., Lee, J., 2022. Silica nanoparticles derived from *Arundo donax L*. ash composite with Titanium dioxide nanoparticles as an efficient nanocomposite for photocatalytic degradation of dye, Chemosphere, 307, 135951.

Farrag, M., 2022. Electrostatic adsorption of ultra-small silver nanoclusters on titanium dioxide modified mesoporous MCM-41 as a high performance photocatalyst for wastewater treatment, Journal of Photochemistry and Photobiology, A: Chemistry, 422, 113551.

Freundlich, H. M. F., 1906. Over the adsorption in solution, Journal of Physical Chemistry, 57, 385–471.

Gong, L., Wu, W., Lin, D., Yang, D. 2021. A superhydrophobic and porous polymer adsorbent with large surface area, Journal of Materials Chemistry, A, 9, 254-258.

Gong, J-L., Wang, X-Y., Zeng, G-M., Chen, L., Deng, J-H., Zhang, X-R., Ni, Q-Y. 2012. Copper (II) removal by pectin–iron oxide magnetic nanocomposite adsorbent Chemical Engineering Journal, 185 – 186, 100 – 107

Gul, A., Ma’amor, A., Khaligh, N. G., Julkapli, N. M., 2022. Recent advancements in the applications of activated carbon for the heavy metals and dyes removal Chemical Engineering Research and Design, 186, 276-299.

Gupta, V. K., Nayak, A., 2012. Cadmium removal and recovery from aqueous solutions by novel adsorbents prepared from orange peel and Fe_2O_3 nanoparticles, Chemical Engineering Journal, 180, 81-90.

Husien, S., El-taweel, R-M., Salim, A. I., Fahim, I. S., Said, L. A., Radwan, A. G., 2022. Review of activated carbon adsorbent material for textile dyes removal: Preparation, and modelling, Current Research in Green and Sustainable Chemistry, 5, 2022, 100325.

Ifguis, O., Ziat, Y., Ammou, F., Bouhdadi, R., Mbarki, M., Benchagra, M., 2022. Theorithecal and experimental study on the thermodynamic parameters and adsorption of methylene blue on "*Argania* shells" in industrial waters South African Journal of Chemical Engineering, 41, 211-222.

Ivanets, A., Prozorovich, V., Roshchina, M., Sychova, O., Srivastava, V., Sillanpää, M., 2022. Methylene blue adsorption on magnesium ferrite: Optimization study, kinetics and reusability, Materialstoday Communications, 31, 103594.

Jayawardena, R., Eldridge, D. S., Malherbe, F., 2022. Sonochemical synthesis of improved graphene oxide for enhanced adsorption of methylene blue, Colloids and Surfaces A: Physicochemical and Engineering Aspects, 650, 129587.

Jawad, A. H., AbdMalek, N. N., Khadiran, T., ALOthman, Z. A., Yaseen, Z. M., 2022. Mesoporous high-surface-area activated carbon from biomass waste via microwave-assisted-H3PO4 activation for methylene blue dye adsorption: An optimized process, Diamond and Related Materials, 128, 109288.

Joshiba, G. J., Senthil, P. S., Govarthanan, M., Ngueagni, P. T., Abilarasu, A., Femina, C. C., 2021. Investigation of magnetic silica nanocomposite immobilized *Pseudomonas fluorescens* as a biosorbent for the effective sequestration of Rhodamine B from aqueous systems. Environmental Pollution, 269,116173.

Joshiba, G. J., Kumar, P. S., Rangasamy, G., Ngueagni, P. T., Pooja, G., Balji, G. B., Alagumalai, K., El-Serehy, H. A., 2022. Iron doped activated carbon for effective removal of tartrazine and methylene blue dye from the aquatic systems: Kinetics, isotherms, thermodynamics and desorption studies, Environmental Research, 215, 114317.

Kamaraj, M., Nithya, T. G., Shyamalagowri, S., Aravind, J., Mythili, R., 2022. Activated carbon derived from almond tree dry leaves waste for enhanced multi dye removal from aqueous solutions, Materials Letters, 308, 131216.

Kaya, Mustafa, Ömer Azahin, and Cafer Saka. 2018. "Preparation and TG/DTG, FT-IR, SEM, BET Surface Area, Iodine Number and Methylene Blue Number Analysis of Activated Carbon from Pistachio Shells by Chemical Activation." International Journal of Chemical Reactor Engineering 16, 2.

Koyuncu, H., Kul, A. R., 2020. Biosorption study for removal of methylene blue dye from aqueous solution using a novel activated carbon obtained from nonliving lichen (*Pseudevernia furfuracea* (L.) Zopf.), Surfaces and Interfaces, 19, 100527.

Langmuir, I., 1916. The constitution and fundamental properties of solids and liquids, Journal of the American Chemical Society, 38, 2221-2295.

León, Andrea, Patricia Reuquen, Carolina Garín, Rodrigo Segura, Patricio Vargas, Paula Zapata, and Pedro A. Orihuela. 2017. "FTIR and Raman Characterization of TiO2 Nanoparticles Coated with Polyethylene Glycol as Carrier for 2-Methoxyestradiol." Applied Sciences, 7, 48.

764 Leyva-Ramos, R., Salazar-Rábago, J. J., Ocampo-Pérez, R., 2021. A novel intraparticle mass
765 transfer model for the biosorption rate of methylene blue on white pine (Pinus durangensis)
766 sawdust. Diffusion-permeation, Chemical Engineering Research and Design, 172, 43-52.
767 Li, H., Budarin, V. L., Clark, J. H., North, M., Wu, X., 2022. Rapid and efficient adsorption of
768 methylene blue dye from aqueous solution by hierarchically porous, activated starbons®:
769 Mechanism and porosity dependence, Journal of Hazardous Materials, 436, 129174.
770 Liu, X-J., Li, F-M., Singh, S., K., 2021. Manganese-modified lignin biochar as adsorbent for
771 removal of methylene blue. Journal of Materials Research and Technology, 12, 1434-1445.
772 Liu, Y., Yuan, Y., Wang, Z., Wen, Y., Liu, L., Wang, T., Xie, X., 2022a. Removal of ofloxacin
773 from water by natural ilmenite-biochar composite: A study on the synergistic adsorption
774 mechanism of multiple effects, Bioresource Technology, 363, 127938.
775 Liu, B., Finkel, M., Grathwohl, P., 2022b. First order approximation for coupled film and
776 intraparticle pore diffusion to model sorption/desorption batch experiments, Journal of,
777 Hazardous Materials, 429, 128314.
778 Liu, B., Finkel, M., Grathwohl, P., 2022. First order approximation for coupled film and
779 intraparticle pore diffusion to model sorption/desorption batch experiments, Journal of,
780 Hazardous Materials, 429, 128314.
781 Madduri, S., Elsayed, I., Hassan, E. B., 2022. Novel Oxone treated hydrochar for the removal of
782 Pb(II) and methylene blue (MB) dye from aqueous solutions, Chemosphere, 20, 127683.
783 Manohara, H. M., Nayak, S. S., Franklin, G., Nataraj, S. K., Mondal, D., 2021. Progress in marine
784 derived renewable functional materials and biochar for sustainable water purification,
785 Green Chemistry, 23, 8305-8331.
786 Masoudian, N., Rajabi, M., Ghaedi, M., 2022. Titanium oxide nanoparticles loaded onto activated
787 carbon prepared from bio-waste watermelon rind for the efficient ultrasonic-assisted
788 adsorption of congo red and phenol red dyes from wastewaters, Polyhedron, 173, 114105.
789 Mohammed, Adnan A., Ziad T. Khodair, and Anees A. Khadom. 2020. “Preparation and
790 Investigation of the Structural Properties of α-Al2O3 Nanoparticles Using the Sol-Gel
791 Method.” Chemical Data Collections 29, 100531.
792 Moradi, O., Pudineh, A., Sedaghat, S., 2022. Synthesis and characterization Agar/GO/ZnO NPs
793 nanocomposite for removal of methylene blue and methyl orange as azo dyes from food
794 industrial effluents, Food and Chemical Toxicology, 169, 113412.
795 Mpatani, F. M., Aryee, A. A., Guo, Q., Dovi, E., Qu, L., , Li, Z., , Han, R., 2020. Uptake of
796 micropollutant-bisphenol A, methylene blue and neutral red onto a novel bagasse-β-
797 cyclodextrin polymer by adsorption process, Chemosphere, 259, 127439.
798 Mu, Z., Liu, D., Lv, J., Chai, D-F., Bai, L., Zhang, Z., Dong, G., Li, J., Zhang, W., 2022. Insight
799 into the highly efficient adsorption towards cationic methylene blue dye with a
800 superabsorbent polymer modified by esterified starch, Journal of Environmental Chemical
801 Engineering, 10, 108425.
802 Mugundan, S, Rajamannan, B., Viruthagiri, G., Shanmugam, N., Gobi, R., Praveen, P., 2015.
803 Synthesis and Characterization of Undoped and Cobalt-Doped TiO_2 Nanoparticles via Sol-
804 Gel Technique, Applied Nanoscience, 5, 449-456.
805 Nagalakshmi, T.V., K.A. Emmanuel, Ch. Suresh Babu, Ch. Chakrapani, and P. Paul Divakar.
806 2015. Preparation of Mesoporous Activated Carbon from Jackfruit PPI-1 Waste and
807 Development of Different Surface Functional Groups, International Letters of Chemistry,
808 Physics and Astronomy 54, 189–200.

Obayomi, K. S., Oluwadiya, A. E., Lau, S. Y., Dada, A. O., Akubuo-Casmir, D., Adelani-Akande, T. A., Bari, A.S.M.F., Temidayo, S. O., Rahman, M. M., 2021. Biosynthesis of Tithonia diversifolia leaf mediated Zinc Oxide Nanoparticles loaded with flamboyant pods (Delonix regia) for the treatment of Methylene Blue Wastewater, Arabian Journal of Chemistry, 14, 103363.

Obayomi, Lau, S. Y., Akubuo-Casmir, D., Yahya, M. D., Auta, M., Bari, A. S. M. F., Oluwadiya, A. E., Obayomi, O. V., Rahman, M. M., 2022. Adsorption of endocrine disruptive congo red onto biosynthesized silver nanoparticles loaded on *Hildegardia barteri* activated carbon, Journal of Molecular Liquids, 352, 118735.

Pamei, M., Achumi, A. G., Kahmei, R., Sarkar, A., Puzari, A., 2022. Functionalized copper metal-organic framework with peroxidase-mimetic activity as an adsorbent for efficient removal of noxious organic dye from aqueous solution, Microporous and Mesoporous Materials, 340, 112031.

Peñas-Garzón, Manuel, Almudena Gómez-Avilés, Jorge Bedia, Juan J. Rodriguez, and Carolina Belver. 2019. "Effect of Activating Agent on the Properties of TiO_2 /Activated Carbon Heterostructures for Solar Photocatalytic Degradation of Acetaminophen." Materials 12, 2030378.

Pi, S., Li, A., Cui, D., Su, Z., Feng, L., Ma, F., Yang, J., 2018. Biosorption behavior and mechanism of sulfonamide antibiotics in aqueous solution on extracellular polymeric substances extracted from *Klebsiella* sp. J1, Bioresource Technology, 272, 346-350.

Priyan, V. V., Kumar, N., Narayanasamy, S., 2022. Toxicological assessment and adsorptive removal of lead (Pb) and Congo red (CR) from water by synthesized iron oxide/activated carbon (Fe_3O_4/ AC) nanocomposite, Chemosphere 294, 133758.

Rahmayanti, M., Syakina, A. N., Fatimah, I., Sulistyaningsih, T., 2022. Green synthesis of magnetite nanoparticles using peel extract of jengkol (*Archidendron pauciflorum*) for methylene blue adsorption from aqueous media, Chemical Physics Letters, 803, 139834.

Reçber, Z. B., Burhan, H., Bayat, R., Nas, M. S., Calimli, M. H., Demirbas, O., Şen, F., Hassan, K. M., 2022. Fabrication of activated carbon supported modified with bimetallic-platin ruthenium nano sorbent for removal of azo dye from aqueous media using enhanced ultrasonic wave, Environmental Pollution, 302, 119033.

Rheima, A. M., Khadom, A. A., Kadhim, M. M., Removal of Cibacron Blue P-6B dye from aqueous solution using synthesized anatase titanium dioxide nanoparticles: Thermodynamic, kinetic, and theoretical investigations, Journal of Molecular Liquids, 357, 119102

Saravanan, A., Kumar, P. S., Jeevanantham, S., Karishma, S., Tajsabreen, B., Yaashikaa, P. R., Reshma, B., 2021. Effective water/wastewater treatment methodologies for toxic pollutants removal: processes and applications towards sustainable development, Chemosphere, 280, 130595.

Shaikh, W. A., Islam, R. U., Chakraborty, S., 2021. Stable silver nanoparticle doped mesoporous biochar-based nanocomposite for efficient removal of toxic dyes, Journal of Environmental Chemical Engineering, 9, 104982.

Sharma, K., Ali, M., Singh, R., Majhi, S., Sharma, S., Tripathi, C. S. P., Guin, D., 2022a. Silver nanoparticles decorated on graphene oxide modified polyester fabric: Catalytic reduction of 4-nitrophenol, organic dyes and SERS application, Journal of Physics and Chemistry of Solids, 165, 110640.

Sharma, A. K., Gupta, A., Dhiman, A., Garg, M., Mishra, R., Agrawal, G., 2022b. Fe_3O_4 embedded κ-carrageenan/sodium alginate hydrogels for the removal of basic dyes, Colloids and Surfaces A: Physicochemical and Engineering Aspects, 654, 130155.

Singh, A., Pal, D. B., Mohammad, A., Alhazmi, A., Haque, S., Yoon, T., Srivastava, N., Gupta, V. K., 2022. Biological remediation technologies for dyes and heavy metals in wastewater treatment: new insight, Bioresource Technology, 343, 16154.

Sips, R., 1948. Combined form of Langmuir and Freundlich equations, Journal of Chemical Physics, 16, 490-495.

Soleymanzadeh, M., Arshadi, M., Salvacion, J.W.L., SalimiVahid, F. 2015. A new and effective nanobiocomposite for sequestration of Cd(II) ions: Nanoscale zerovalent iron supported on sineguelas seed waste, Chemical Engineering Research and Design, 93, 696-709.

Subhan, F., Aslam, S., Yan, Z., Yaseen, M., Naeem, M., Ikram, M., Ali, A., Bibi, S., 2022. Adsorption and reusability performance of hierarchically porous silica (MMZ) for the removal of MB dye from water, Inorganic Chemistry Communications, 139, 109380.

Sunny, N. E., Mathew, S. S., Chandel, N., Saravanan, P., Rajeshkannan, R., Rajasimman, M., Vasseghian, Y., Rajamohan, N., Kumar, S. V., 2022. Green synthesis of titanium dioxide nanoparticles using plant biomass and their applications- A review, Chemosphere, 300, 134612.

Tamer, Y., Koşucu, A., Berber, H., 2022. Graphene oxide incorporated chitosan/acrylamide/itaconic acid semi-interpenetrating network hydrogel bio-adsorbents for highly efficient and selective removal of cationic dyes, International Journal of Biological Macromolecules, 219, 273-289.

Tempkin, M. I., Pyzhev, V., 1904. Kinetics of ammonia synthesis on promoted iron catalyst, Acta physicochimica URSS, 12, 327–356.

Thanh, N. C., Shanmugam, S., Shanmugasundaram, S., AlSalhi, M. S., Devanesan, S., Shanmuganathan, R., 2022. Chi, N. T. L., Comparison of *Simarouba glauca* seed shell carbons for enhanced direct red 12B dye adsorption: Adsorption isotherm and kinetic studies, Food and Chemical Toxicology, 168, 113326.

Toth, 1971. State equations of the solid gas interface layer, Acta Chimica (Academiae Scientiarum) Hungaricae, 69, 311-317.

Tran, T. H., Le, A. H., Pham, Duong, L. D., Nguyen, X. C., Nadda, A. K., Chang, S. W., Chung, W. J., Nguyen, D. D., Nguyen, D. T., 2022. A sustainable, low-cost carbonaceous hydrochar adsorbent for methylene blue adsorption derived from corncobs, Environmental Research, 212, 113178.

Valdés-Rodríguez, E.M., D.I. Mendoza-Castillo, H.E. Reynel-Ávila, I.A. Aguayo-Villarreal, and A. Bonilla-Petriciolet. 2022. Activated carbon manufacturing via alternative mexican lignocellulosic biomass and their application in water treatment: preparation conditions, surface chemistry analysis and heavy metal adsorption properties." Chemical Engineering Research and Design, 187, 9–26.

Wang, Y., Zhao, L., Hou, J., Peng, H., Wu, J., Liu, Z., Guo, X., 2018. Kinetic, isotherm, and thermodynamic studies of the adsorption of dyes from aqueous solution by cellulose-based adsorbents. Water Science and Technology. 77, 2699–2708.

Widiyastuti, W., Rois, M. F., Suari, N. M. I. P., Setyawan, H., 2020. Activated carbon nanofibers derived from coconut shell charcoal for dye removal application, Advanced Powder Technology, 31, 3267-3273.

Xue, H., Wang, X., Xu, Q., Dhaouadi, F., Sellaoui, L., Seliem, M. K., Lamine, A. B., Belmabrouk, H., Bajahzar, A., Bonilla-Petriciolet, A., Li, Z., Li, Q., 2022. Adsorption of methylene blue from aqueous solution on activated carbons and composite prepared from an agricultural waste biomass: A comparative study by experimental and advanced modeling analysis, Chemical Engineering Journal, 430 (2), 132801.

Yadav, S. K., Dhakate, S. R., Singh, B. P., 2021. Carbon nanotube incorporated eucalyptus derived activated carbon-based novel adsorbent for efficient removal of methylene blue and eosin yellow dyes, Bioresource Technology, 344, 126231.

Yadav, S., Asthana, A., Singh, A. K., Patel, J., Sreevidya, S., Carabineiro, S. A. C., 2022. Facile preparation of methionine-functionalized graphene oxide/chitosan polymer nanocomposite aerogel for the efficient removal of dye and metal ions from aqueous solutions, Environmental Nanotechnology, Monitoring and Management, 18, 100743.

Yar, A., Parlayici, S., 2022. Carbon nanotubes/ polyacrylonitrile composite nanofiber mats for highly efficient dye adsorption, Colloids and Surfaces A: Physicochemical and Engineering Aspects, 651, 129703.

Zeng, H., Qi, W., Zhai, L., Wang, F., Zhang. J., Li, D., 2022. Magnetic biochar synthesized with waterworks sludge and sewage sludge and its potential for methylene blue removal, Journal of Environmental Chemical Engineering, 9, 105951.

Zhang, Yufan, Fan Fu, Yuzhou Li, Desuo Zhang, and Yuyue Chen. 2018. "One-Step Synthesis of Ag@TiO_2 Nanoparticles for Enhanced Photocatalytic Performance." Nanomaterials 8, 12.

Zhang, Y., Zhao, Y-P., Qiu, L-L., Xiao, J., Wu, F-P., Cao, J-P., Bai, Y-H., Liu, F-J., 2022a. Insights into the KOH activation parameters in the preparation of corncob-based microporous carbon for high-performance supercapacitors, Diamond and Related Materials, 129, 109331.

Zhang, L., Feng, G., Zhou, W., Zhang, Y., Wang, L., Wang, L., Liu, Z., Zhao, T., Zhu, W., Zhang, B., 2022b. Core-shell sp^3@sp^2 nanocarbon for adsorption of anionic and cationic organic dyes: Effect of the graphitization of nanocarbon, Colloids and Surfaces A: Physicochemical and Engineering Aspects, 651, 129694.

Zhang, S., Fan, X., Xue, J., 2023. A novel magnetic manganese oxide halloysite composite by one-pot synthesis for the removal of methylene blue from aqueous solution, Journal of Alloys and Compounds, 930, 167050.

Zhu, R., Xia, J., Zhang, H., Kong, F., Hu, X., Shen, Y., Zhang, W-H., 2021. Synthesis of magnetic activated carbons from black liquor lignin and Fenton sludge in a one-step pyrolysis for methylene blue adsorption, Journal of Environmental Chemical Engineering, 9, 106538.